Structured surface reflector design for oblique incidence beam splitter at 610 GHz

Fabien Defrance, Massimiliano Casaletti, Julien Sarrazin, Martina Wiedner, Hugh Gibson, Gregory Gay, Roland Lefevre, Yan Delorme

Structured surface reflector design for oblique incidence beam splitter at 610 GHz

F. Defrance,[1,*] M. Casaletti,[2] J. Sarrazin,[2] M.C. Wiedner,[1] H. Gibson,[3] G. Gay,[1] R. Lefèvre,[1] and Y. Delorme[1]

[1]*Observatoire de Paris, Laboratory for Studies of Radiation and Matter in Astrophysics, 61 av de l'Observatoire, 75014 Paris, France*
[2]*Laboratoire d'Electronique et Electromagnétisme, Sorbonne Universités, UPMC Univ Paris 06, UR2, L2E, F-75005 Paris, France*
[3]*Gibson Microwave design, 9 rue Pasteur, 92160 Antony, FRANCE*
[*]*fabien.defrance@obspm.fr*

Abstract: An iterative alternate projection-based algorithm is developed to design structured surface reflectors to operate as beam splitters at GHz and THz frequencies. To validate the method, a surface profile is determined to achieve a reflector at 610 GHz that generates four equal-intensity beams towards desired directions of ±12.6° with respect to the specular reflection axis. A prototype is fabricated and the beam splitter behavior is experimentally demonstrated. Measurements confirm a good agreement (within 1%) with computer simulations using Feko™, validating the method. The beam splitter at 610 GHz has a measured efficiency of 78% under oblique incidence illumination that ensures a similar intensity between the four reflected beams (variation of about 1%).

OCIS codes: (050.2770) Gratings; (050.5080) Phase shift; (260.2110) Electromagnetic optics; (350.1270) Astronomy and astrophysics; (040.2235) Far infrared or terahertz; (040.2840) Heterodyne.

References and links

1. G. Beaudin and P. J. Encrenaz, "Fundamentals of receivers for terahertz systems," in *New Directions in Terahertz Technology*, J. M. Chamberlain and R. Miles, eds. (Academic, 1997), pp. 53-61.
2. F. P. Helmich on behalf of the HIFI consortium, "Herschel-hifi: The heterodyne instrument for the far-infrared," EAS Publications series **52**, 15–20 (2011).
3. J. N. Mait, "Understanding diffractive optic design in the scalar domain," J. Opt. Soc. Am. A **12**, 2145–2158 (1995).
4. R. Guesten, G. A. Ediss, F. Gueth, K. H. Gundlach, H. Hauschildt, C. Kasemann, T. Klein, J. W. Kooi, A. Korn, I. Kramer, H. G. LeDuc, H. Mattes, K. Meyer, E. Perchtold, M. Pilz, R. Sachert, M. Scherschel, P. Schilke, G. Schneider, J. Schraml, D. Skaley, R. Stark, W. Wetzker, H. Wiedenhover, W. Wiedenhover, S. Wongsowijoto, F. Wyrowski, "CHAMP, The carbon heterodyne array of the MPIFR," Proc. SPIE **3357**, 167-177 (1998).
5. U. U. Graf, S. Heyminck, E. A. Michael, S. Stanko, C. E. Honingh, K. Jacobs, R. T. Schieder, J. Stutzki, and B. Vowinkel, "SMART: The KOSMA sub-millimeter array receiver for two frequencies," Proc. SPIE **4855,** 322–329 (2003).
6. C. Risacher, R. Güsten, J. Stutzki, H. W. Hübers, P. Pütz, A. Bell, D. Büchel, I. Camara, R. Castenholz, M. Choi, U. Graf, S. Heyminck, C. Honingh, K. Jacobs, M. Justen, B. Klein, T. Klein, C. Leinz, N. Reyes, H. Richter, O. Ricken, A. Semenov, A. Wunsch, "The upGREAT heterodyne array receivers for far infrared astronomy," presented at the 39th International Conference on Infrared, Millimeter, and Terahertz waves (IRMMW-THz), Tucson, USA, 14-19 September 2014.
7. H. Dammann and E. Klotz, "Coherent optical generation and inspection of two-dimensional periodic structures," Optica Acta **24**(4), 505–515 (1977).
8. J. Wang, C. Zhou, J. Ma, F. Zhu and W. Huang, "High Efficient Reflective Dammann Grating," in *Imaging and Applied Optics 2014*, OSA Technical Digest (online) (Optical Society of America, 2014), paper JTu4A.19.
9. J. N. Mait, "Design of Dammann gratings for two-dimensional, nonseparable, noncentrosymmetric responses," Opt. Lett. **14**, 196-198 (1989).
10. S. J. Walker and J. Jahns, "Array generation with multilevel phase gratings," J. Opt. Soc. Am. A **7**, 1509-1513 (1990).
11. U. U. Graf and S. Heyminck, "Fourier gratings as submillimeter beam splitters," IEEE Trans. on Antennas and Propagation **49**(4), 542–546 (2001).

12. J. N. Mait, "Design of binary-phase and multiphase Fourier gratings for array generation," J. Opt. Soc. Am. A **7**, 1514-1528 (1990).
13. S. Heyminck and U. U. Graf, “Array-receiver LO unit using collimating Fourier-gratings,” in *Proceedings of the 12th International Symposium on Space Terahertz Technology*, I. Mehdi, ed. (Jet Propulsion Laboratory, 2001), pp. 563–570.
14. V. Arrizón, M. Testorf, S. Sinzinger, and J. Jahns, "Iterative optimization of phase-only diffractive optical elements based on a lenslet array," J. Opt. Soc. Am. A **17**, 2157-2164 (2000).
15. G. Zhou, Y. Chen, Z. Wang, and H. Song, "Genetic local search algorithm for optimization design of diffractive optical elements," Appl. Opt. **38**, 4281-4290 (1999).
16. M. E. Testorf and M. A. Fiddy,"Efficient optimization of diffractive optical elements based on rigorous diffraction models," J. Opt. Soc. Am. A **18**, 2908-2914 (2001).
17. J. N. Mait, D. W. Prather, and M. S. Mirotznik, "Design of binary subwavelength diffractive lenses by use of zeroth-order effective-medium theory," J. Opt. Soc. Am. A **16**, 1157-1167 (1999).
18. R. W. Gerchberg and W. O. Saxton, “A practical algorithm for the determination of the phase from image and diffraction plane pictures,” Optik **35**(2), 237-246, (1972).
19. R. Piestun and J. Shamir, “Synthesis of three-dimensional light fields and applications,” in *Proceedings of the IEEE* **90**(2), 222–244, (2002).

1. Introduction

Heterodyne receivers [1] are an essential part of radio-astronomy. They can achieve very high spectral resolution and are therefore well suited to observe molecular and atomic transition lines, from which physical and chemical conditions of the interstellar medium can be determined, as well as its kinematics. In heterodyne receivers, the observed sky signal, also called radio frequency (RF) signal, is mixed with an artificial monochromatic signal created by a local oscillator (LO) in order to shift the frequency of the sky signal to a much lower frequency without losing any amplitude or frequency information (Fig. 1). The down-converted signal at the output of the mixer is called intermediate frequency (IF) signal. This feature is particularly interesting in THz astronomy because it enables down-converting an RF signal observed at a few THz, to a few GHz, and to process it more easily with high spectral resolution.

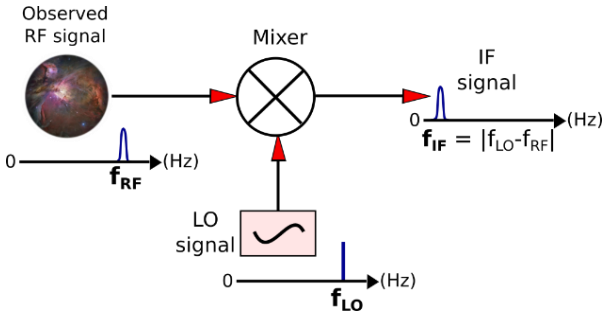

Fig. 1. Down-conversion of the RF signal in a heterodyne receiver.

Classic THz heterodyne systems exhibit high spectral resolution (with many spectral channels). However, these systems are usually limited to a single spatial pixel (e.g. HIFI instrument on Herschel satellite [2]). Recently, there has been a growing interest among scientists in developing multiple-pixel THz radio-astronomy instruments. To that purpose, arrays of heterodyne receivers are being developed to simultaneously measure spectra at several positions in the sky. In this configuration, each pixel includes a mixer. So, observing the sky with multiple pixels involves pumping multiple mixers with a LO. The most efficient way to do so is to split the LO beam into several beams, each illuminating one of the mixers. Phase gratings [3] are the perfect tool for achieving this goal and are already used in some receivers (e.g. CHAMP, SMART, upGREAT [4-6]). To the authors’ best knowledge, only two kinds of phase gratings are used in THz heterodyne receivers: stepped phase gratings and Fourier gratings. Stepped phase gratings, such as Dammann gratings [7-10], exhibit discrete level step profiles, while Fourier gratings are generated by Fourier series and therefore exhibit a continuous geometry

[11-13]. Both gratings are periodic and have a constrained geometry, which limits the beam patterns that can be efficiently achieved. These limitations can lead to a non-optimal distribution of LO power, especially when considering the geometry constraints of the multiple heterodyne receiver arrangement within the instrument. The beam splitter proposed in this paper is based on a structured surface reflector that has been designed to overcome these limitations. It demonstrates the capability to split an oblique incident beam into four similar-intensity beams towards desired directions. To that aim, an iterative design algorithm that takes into account the dipolar behavior of the equivalent magnetic current radiation was developed. This ensures the four generated beams to have identical power density under oblique incidence beam illumination while reaching a high overall efficiency in the THz domain. The concept has been proved with a reflector that is designed and fabricated, and for which both simulation and measurement results confirm its operation at 610 GHz.

2. Structured surface reflector design procedure

Different optimization methods to design phase only Diffractive Optical Elements (DOEs) already exist in the literature [14-19] where the Inverse Fourier Transform (IFT) maps the desired radiated field pattern onto the DOE aperture. An iterative process based on alternate projections involving both IFT and FT is then used to converge to an aperture distribution that matches both the desired radiated field pattern and the DOE's physical constraints. In the process, Geometrical Optics (GO) approximation is classically assumed at optical frequencies but can lead to non-optimized performance at THz. The beam splitter design procedure presented in this paper does not make use of GO approximation but calculates instead the radiated field due to an equivalent magnetic current in the DOE aperture. The geometry of the problem is shown in Fig 2. The origin of the reference system is placed at the aperture center with the *z*-axis normal to the aperture. A time dependence $e^{j\omega t}$, $\omega = 2\pi f$ being the angular frequency, is assumed and suppressed. The tangential electric field on the radiating aperture is expressed as $\mathbf{E}_A(x',y') = E_A(x',y')\hat{\mathbf{p}}$, where the unit vector $\hat{\mathbf{p}}$ is supposed constant along the aperture.

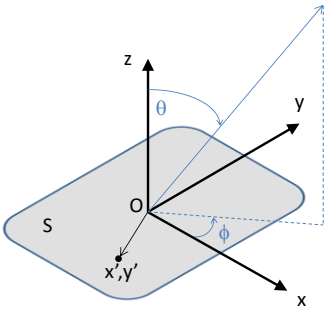

Fig. 2. Geometry of the problem.

The far-field radiated by the aperture is related to the tangential aperture field by the relation

$$\mathbf{E}_{FF}(\theta,\phi) = \mathbf{F}^{md}(\theta,\phi)\tilde{E}_A\left(k\sin(\theta)\cos(\phi), k\sin(\theta)\sin(\phi)\right), \quad \theta\in[0,\pi],\ \phi\in[0,2\pi) \qquad (1)$$

where θ,ϕ are the angular spherical coordinates, k is the wave number, $\tilde{E}_A(k_x,k_y) = \mathbb{F}\{E_A(x',y')\}$ is the 2D spatial Fourier transformation of the complex amplitude of the aperture field, and $\mathbf{F}^{md}(\theta,\phi)$ is the radiation pattern of a magnetic dipole oriented along $\hat{\mathbf{p}}$:

$$\mathbf{F}^{md}(\theta,\phi) = jk\sin\theta\left(\hat{\mathbf{y}}\cos\phi - \hat{\mathbf{x}}\sin\phi\right)\times\hat{\mathbf{p}} \qquad (2)$$

The goal of the design procedure is to find the optimal aperture distribution $E_{Atarget}(x',y')$ able to radiate a desired target radiation pattern $\mathbf{M}(\theta,\phi)$ that can be implemented using reflective elements. This latter condition allows us to limit our attention to an aperture field of the following form

$$E_A(x',y')\hat{\mathbf{p}} = r^{\perp}(x',y')\mathbf{E}^{\perp}_{inc}(x',y') + r^{\parallel}(x',y')\mathbf{E}^{\parallel}_{inc}(x',y') \tag{3}$$

where $\mathbf{E}^{\perp}_{inc}, \mathbf{E}^{\parallel}_{inc}$ are the orthogonal and parallel component of the incident wave with respect to the incident plane, and $r^{\perp}, r^{\parallel}$ are the corresponding complex local reflection coefficients such that $|r^{\perp}| = |r^{\parallel}| = 1$.

Without loss of generality let us assume that the incident beam has just one polarization component. Under this assumption the aperture field amplitude is directly dictated by the incident beam:

$$|\mathbf{E}_A(x',y')| = |E_{inc}(x',y')| \tag{4}$$

The target far-field radiation pattern weighted by the dipole radiation pattern $M(\theta,\phi)/F^{md}(\theta,\phi)$ is firstly mapped onto the aperture field spectra via the transformation

$$\tilde{T}(k_x,k_y) = \frac{M\left(\theta_{k_x,k_y},\phi_{k_x,k_y}\right)}{F^{md}\left(\theta_{k_x,k_y},\phi_{k_x,k_y}\right)}\ ,\ \theta_{k_x,k_y} = \sin^{-1}\left(\frac{\sqrt{k_x^2+k_y^2}}{k}\right),\ \phi_{k_x,k_y} = \tan^{-1}\left(\frac{k_y}{k_x}\right) \tag{5}$$

It is important to remark that Eq. (4) defines the spectrum only in the circular spectral region defined by $\sqrt{k_x^{\ 2}+k_y^{\ 2}} \le k_0$ (visible region). The spectrum outside the visible region can be arbitrarily chosen, and represents a degree of freedom in the optimization process. The steps performed to obtain the optimal aperture distribution $E_A(x',y')$ are illustrated in Fig. 3.

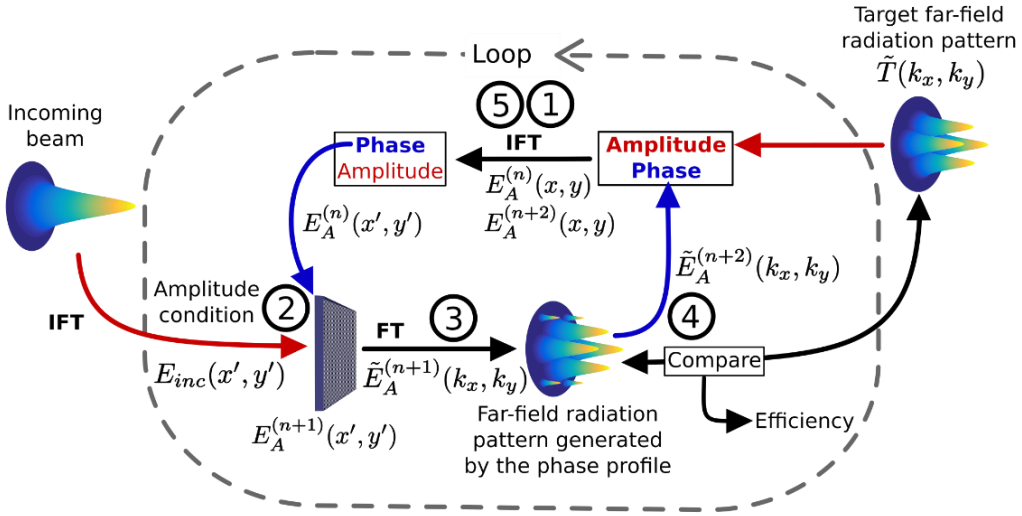

Fig. 3. Schematic of the algorithm calculating the phase profile of the structured surface reflector.

1. The starting aperture distribution can be arbitrarily selected. A possible choice is to use the IFT of the target function $\tilde{T}$:

$$E_A^{(0)}(x',y') = \mathbb{F}^{-1}\left\{\tilde{T}(k_x,k_y)\right\} \tag{6}$$

2. The physical realization constraints are considered. The amplitude condition [Eq. (4)] has to be imposed and the aperture field has to be set to zero outside the aperture surface S, namely:

$$E_A^{(1)}(x',y') = \left|E_{inc}(x',y')\right| e^{jArg\left(E_A^{(0)}(x',y')\right)} S(x',y') \tag{7}$$

where $S(x',y') = \begin{cases} 1 & (x',y') \in S \\ 0 & otherwise \end{cases}$.

3. A Fourier Transform is used to calculate the far-field pattern radiated by the aperture field $E_A^{(1)}(x',y')$:

$$\tilde{E}_A^{(1)}(k_x,k_y) = \mathbb{F}\left\{E_A^{(1)}(x,y)\right\} \tag{8}$$

4. The radiation pattern is compared to the spectral target function $\tilde{T}$ inside the visible region. If the radiated field fulfills a desired criterion the algorithm stops. Otherwise a new radiation pattern is generated as:

$$\tilde{E}_A^{(2)}(k_x,k_y) = \tilde{E}_A^{(1)}(k_x,k_y) K(k_x,k_y) \tag{9}$$

where $K(k_x,k_y) = \begin{cases} k(k_x,k_y) & \text{if } \sqrt{k_x^{\,2}+k_y^{\,2}} \le k_0 \\ 0 & \text{otherwise} \end{cases}$ is a function that allows to fit the target function inside the visible region while keeping the invisible region unchanged.

5. A new aperture field is then obtained via an IFT

$$E_A^{(2)}(x',y') = \mathbb{F}^{-1}\left\{\tilde{E}_A^{(2)}(k_x,k_y)\right\} \tag{10}$$

and injected in the loop at point 2.

3. Oblique incidence beam splitter design

We tested the algorithm by designing a structured surface reflector for a Gaussian beam at 610 GHz with a waist of 5 mm, and an oblique incidence of 25° with respect to the surface normal. The target far-field radiation pattern is composed of four Gaussian beams of identical intensity, with an angle of 12.6° between each beam and the specular reflection axis as shown in Fig. 4. As stopping criterion, we impose that the obtained efficiency is larger than a given threshold. The efficiency is defined as the ratio of the power density integrated within the targeted multiple beams and the power of the Gaussian beam impinging over the surface S.

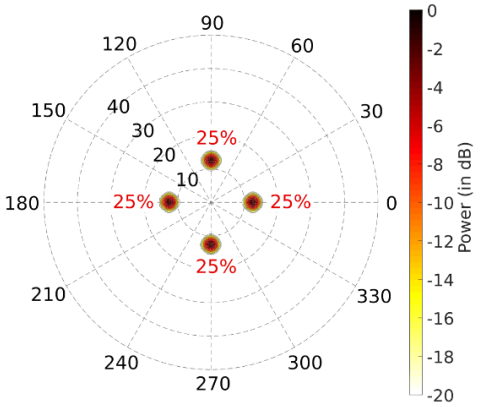

Fig. 4. Target far-field, expressed in percentage of the incident beam's intensity.

3.1 Structured surface profile determination

Since in the optimization procedure the aperture field has been supposed of the form (Eq. (3) - Eq. (4)), the structured surface profile of the reflector is generated in order to implement the following reflection coefficient:

$$r(x',y') = e^{j\left[Arg\left(E_A(x',y')\right) - Arg\left(E_{inc}(x',y')\right)\right]} = e^{j\psi(x',y')} \quad . \tag{11}$$

In our example, a structured surface of dimensions 44.8 mm x 49.4 mm ($91\lambda_0$ x $101\lambda_0$, with λ_0 the free space wavelength at 610 GHz) has been selected to ensure that almost the totality of the incoming energy is reflected by the reflector. Moreover, a periodic profile has been used to facilitate its alignment with respect to the incoming beam. A portion of the phase profile $\psi(x',y')$ obtained using the proposed method is shown in Fig. 5(a), while the corresponding metallic implementation is shown in Fig. 5(b). The total calculation process converged with 50 iterations and took about 1 minute on a 3.5 GHz quad-core desktop computer. In the obtained design, the spatial period is about four times the wavelength.

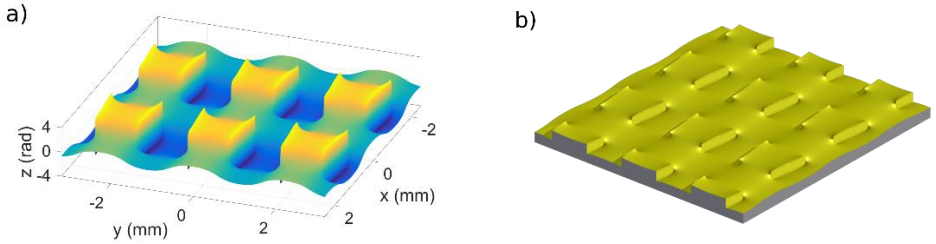

Fig. 5. (a) Phase profile calculated by the algorithm, and (b) corresponding metallic structured surface profile.

3.2 Reflector simulated behavior

The structured surface reflector obtained with the algorithm has been analyzed using the commercial software Feko™ based on a Method of Moments. Due to the structure complexity, the analysis of the whole structure with the available computer was not possible. Thus, only a portion of it has been simulated. The obtained numerical results correctly predict the reflected beam efficiency but not the beam widths. Figure 6(a) shows a field distribution cut-plane while Fig. 6(b) represents the normalized intensity distribution of the four beams 30 cm above the structured surface reflector in polar coordinates, where the origin corresponds to the axis of the specular reflection of the incident beam. The azimuthal angle θ is indicated by the circular lines, while the polar angle φ by the radial lines. Contour levels are separated by steps of 2 dB of the maximum intensity, and the lowest contour level is at -20 dB. The power reflected by the beam splitter is expressed in terms of percentage of the input beam power. The four diffracted beams have almost the same intensities (±1%). Using Feko™ simulation, the obtained beam intensities are respectively 19%, 21%, 20%, and 21%, whereas GO approximation leads to disparity in the intensities as high as 9%. The difference can be explained by the dipolar nature of the reflector's current radiation that is not taken into account in GO, which leads to unbalanced beams under oblique incidence illumination (the intensity of the field radiated by a current element is not isotropic over the beam angles as supposed by GO). The total simulated efficiency of the structured surface reflector is 81%. The simulation was done for a linearly polarized incident beam, as shown in Fig. 6(a). For an orthogonally polarized input beam, the efficiency of each output beam changes of about ±1%, but the total efficiency of the structured surface reflector remains approximately the same.

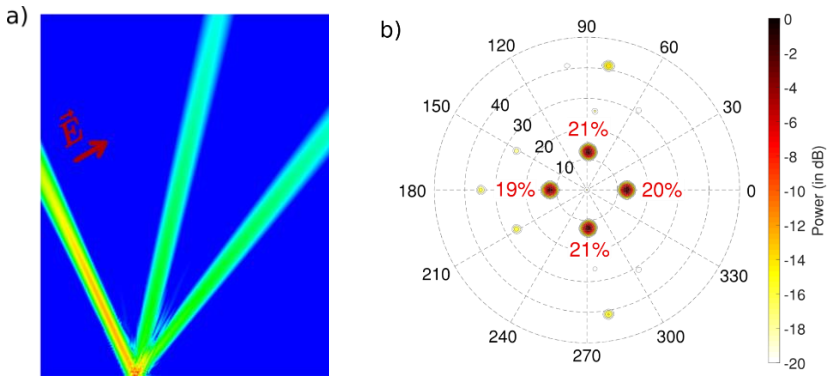

Fig. 6. Analysis of the reflector behavior illuminated by an incident Gaussian beam using Feko™. (a) Field distribution cut-plane including the incident beam (from the left) and two reflected beams. (b) Intensity distribution 30 cm above the structured surface reflector.

The efficiency of the structured surface reflector has also been simulated with Feko™ over the bandwidth 440 GHz – 840 GHz (Fig. 7). The intensities of the four beams have been calculated separately over the bandwidth and the global efficiency of the structured surface reflector was calculated as the sum of the intensities of the four beams. The denomination of the four beams (left, right, up, down) corresponds to the position of these beams in Fig. 6(b). This simulation shows that the intensity of each pair of beams evolves differently. For example, a variation of the intensities of the four beams limited to ±25% of the beams' nominal value at 610 GHz corresponds to the bandwidth 560 GHz – 700 GHz.

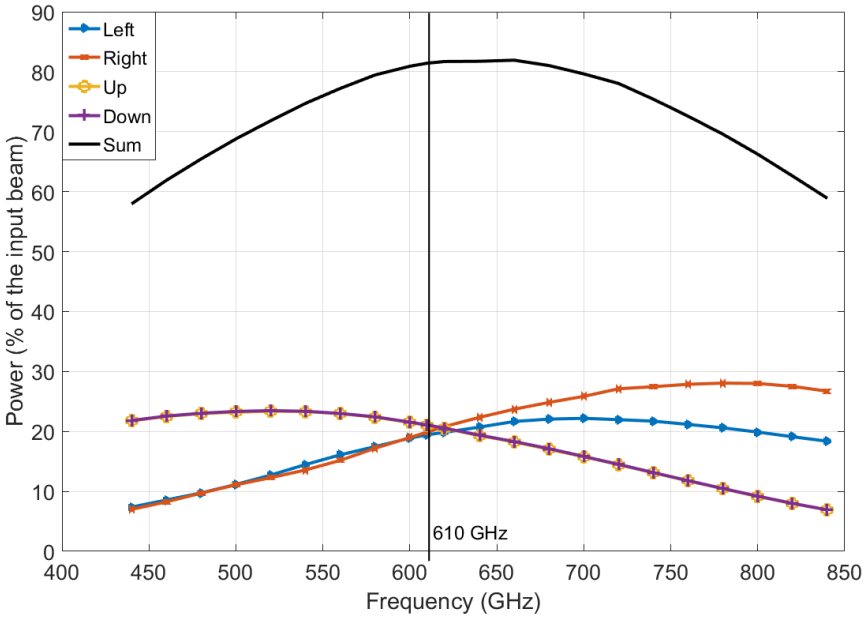

Fig. 7. Efficiency of the structured surface reflector for each of the four beams and for the sum of the intensities of the four beams (black curve), simulated with Feko™.

4. Prototype

To verify our design and confirm the simulations, we fabricated a prototype structured surface reflector and tested it at 610 GHz.

4.1 Mechanical design

The reflector size is 44.8 mm x 49.4 mm and contains 400 cells. It covers more than four times the beam waist of the input Gaussian beam, which is 5 mm, to ensure that at least 99.9% of the beam is reflected. The prototype was made out of brass and milled with a 0.2 mm diameter ball-shaped end mill. Figure 8 shows the manufactured structured surface reflector. The surface of the prototype has been measured with a profilometer (Dektak8), whose precision is better than 0.1 µm. The difference between the manufactured prototype and the theoretical shape is less than 6 µm. The average roughness of the structured surface has also been measured to be below 0.4 µm, which should be low enough to not generate any additional noticeable losses.

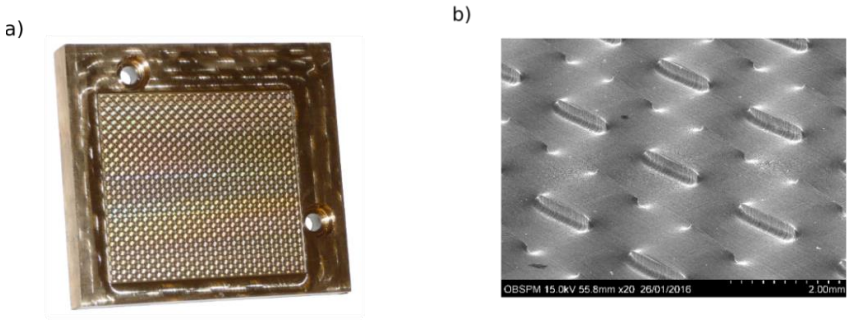

Fig. 8. Pictures of the manufactured structured surface reflector, taken with (a) a camera and (b) a Scanning Electron Microscope (SEM).

4.2 Efficiency measurement

To test the prototype, a 610 GHz source was used to generate the signal and a Golay cell power meter to measure the power of the reflected beams. In order to measure the horizontal radiation pattern, the source and the reflector were fixed on a rotating platform (see Fig. 9). The Golay cell power meter was always set at the same distance from the focusing mirrors so the beams it measured had always the same radius (the beams are diverging along their propagation axis, so it is important to always measure them at the same position to be able to compare their intensity distribution).

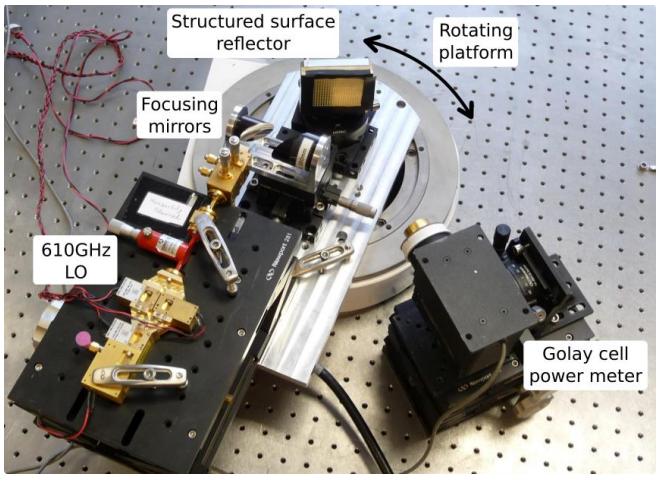

Fig. 9. Experimental set-up to measure the radiation efficiency.

The power received with and without the structured surface reflector was compared in order to determine the relative intensity of each diffracted beam and the overall efficiency (Fig. 10).

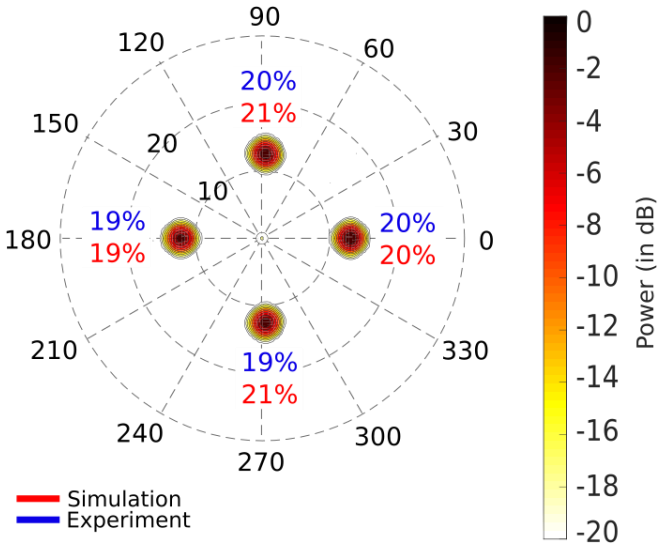

Fig. 10. Measured relative power and position of the 4 beams generated by the prototype (blue numbers), compared with the simulation results (red numbers).

The four beams are approximately equally powerful and their relative intensity is close to the simulation results (maximum 2% difference), as shown in Fig. 9. The accuracy of the measurements is estimated to be ±1%, which takes into account the alignment difficulties, the possible power variations of the source, and the precision of the Golay cell power meter. The total efficiency of this prototype is 78 ± 4%, which is close to the 81% predicted by electromagnetic simulations. The remaining power was measured in the other harmonics generated by the structured surface reflector. Moreover, the reflected beams' directions are very close to the theoretical angles (less than 0.2° difference).

5. Additional simulation results

In order to demonstrate the capability of the iterative algorithm to design structured surfaces able to generate other types of far-field patterns, results of two more examples are here given in simulation. The first one, shown in Fig. 11, is the name of our laboratory (LERMA) and the second one is the drawing of a butterfly (Fig. 12). The iterative algorithm converged in both cases to the appropriate structured surface reflector profiles that generate these patterns. Feko™ simulations are used to check the validity and the efficiency of these two designs, as we did for the four-beam prototype. In these two examples (Figs. 11 and 12) we only considered the case of a normal incident beam. The structured surface reflector profiles generating these two beam patterns are non-periodic and have been integrally used in Feko™ simulations. The size of these structured surface reflector profiles is 39.3 mm x 39.3 mm ($80\lambda_0$ x $80\lambda_0$ at 610 GHz) and the incoming Gaussian beam has a waist of 11 mm.

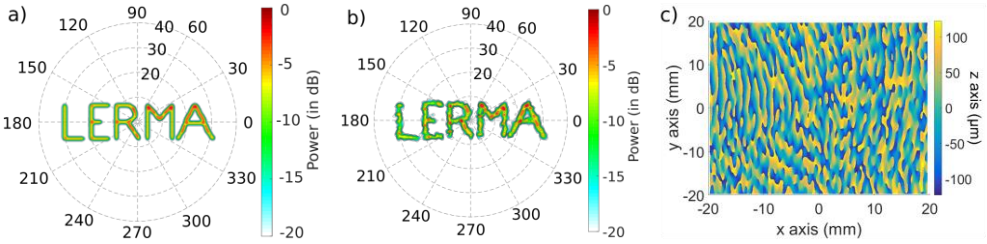

Fig. 11. (a) Normalized target far-field, (b) normalized far-field simulated with Feko™ generated by (c) the structured surface reflector profile.

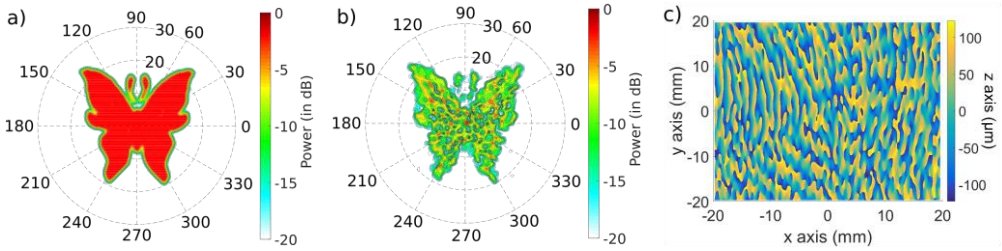

Fig. 12. (a) Normalized target far-field, (b) normalized far-field simulated with Feko™ generated by (c) the structured surface reflector profile.

The iterative algorithm can be used to design structured surface reflector profiles able to efficiently generate a wide range of beam patterns. This result can be reached because, unlike in classical phase gratings used at THz frequencies, our design procedure does not specifically require a periodic structure. Moreover, it has to be emphasized that in the two above examples, no constraint was imposed on the phase of the radiated far-field. Setting a constraint on the phase would reduce the overall intensity efficiency. In the two examples, the normalized intensity is below -20 dB outside the target beam pattern, which indicates that the structured surface reflects most of the power within the target far-field pattern.

6. Conclusion

We have developed an iterative alternate projection-based algorithm to design structured surface reflectors that can be used as beam splitters at GHz and THz wavelengths. The dipolar behavior of current radiation has been considered in the algorithm in order to generate structures able to reflect similar intensity beams under oblique incidence illumination. The commercial electromagnetic software Feko™ is used to fine tune the design and to have a precise estimation of its efficiency. In order to validate our approach, we designed, manufactured, and tested a prototype structured surface reflector for 610 GHz able to split one incoming beam into four beams. The fabricated prototype exhibits an efficiency of 78% with an intensity variation between reflected beams of about 1%, within 2% of the predicted efficiency. This result confirms our algorithm and simulation tool. We are now planning to use this approach to create higher frequency beam splitters for the next generation of multi-pixel THz heterodyne receivers. Moreover, as detailed in section 5, our algorithm can calculate non-constrained and non-periodic structured surface reflectors which are able to generate a wide range of far-field patterns. Actual gratings used in THz heterodyne receivers can reach the same efficiency as the structured surface reflector presented in this article, but as they are periodic and have a constrained shape, they can only generate efficiently a limited number of beam patterns. Although the proposed design procedure is valid for any frequency range, the limitation comes from the manufacturing process used for the prototype. Depending on the desired target far-

field pattern, the structured surface reflectors designs can exhibit a complicated profile and thus cannot be easily fabricated. Moreover, the higher the frequency, the higher the accuracy should be. Above 4 or 5 THz, actual milling techniques do not offer enough accuracy and other techniques like etching should be considered.

Funding

This work was funded by the National Centre for Space Studies (CNES) and the Laboratory for Studies of Radiation and Matter in Astrophysics (LERMA).